ADVANCED MATERIALS
www.advmat.de

Inhibiting Interfacial Nonradiative Recombination in Inverted Perovskite Solar Cells with a Multifunctional Molecule

Jiaxin Wu, Rui Zhu, Guixiang Li, Zuhong Zhang, Jorge Pascual, Hongzhuo Wu, Mahmoud H. Aldamasy, Luyao Wang, Zhenhuang Su, Silver-Hamill Turren-Cruz, Rajarshi Roy, Fahad A Alharthi, Ali Alsalme, Junhan Zhang, Xingyu Gao, Michael Saliba, Antonio Abate, and Meng Li**

Interface-induced nonradiative recombination losses at the perovskite/electron transport layer (ETL) are an impediment to improving the efficiency and stability of inverted (p-i-n) perovskite solar cells (PSCs). Tridecafluorohexane-1-sulfonic acid potassium (TFHSP) is employed as a multifunctional dipole molecule to modify the perovskite surface. The solid coordination and hydrogen bonding efficiently passivate the surface defects, thereby reducing nonradiative recombination. The induced positive dipole layer between the perovskite and ETLs improves the energy band alignment, enhancing interface charge extraction. Additionally, the strong interaction between TFHSP and the perovskite stabilizes the perovskite surface, while the hydrophobic fluorinated moieties prevent the ingress of water and oxygen, enhancing the device stability. The resultant devices achieve a power conversion efficiency (PCE) of 24.6%. The unencapsulated devices retain 91% of their initial efficiency after 1000 h in air with 60% relative humidity, and 95% after 500 h under maximum power point (MPP) tracking at 35 °C. The utilization of multifunctional dipole molecules opens new avenues for high-performance and long-term stable perovskite devices.

1. Introduction

Metal halide perovskites have emerged as promising materials for solar cells due to their high absorption coefficient, low exciton binding energy, long charge carrier diffusion length, tunable bandgap, and cost-effective solution processing.[1–3] Over the past decade, the power conversion efficiency (PCE) of perovskite solar cells (PSCs) has increased from an initial 3.8% to a certified 26.1% on par with silicon.[4] However, interface-induced nonradiative recombination hampers the further development of PSCs, which have two critical interfacial junctions, i.e., the perovskite/electron transport layer (ETL) and perovskite/hole transport layer (HTL) interfaces.[5] The adverse impact of buried perovskite/HTL interface in

J. Wu, R. Zhu, Z. Zhang, H. Wu, M. Li
Key Lab for Special Functional Materials of Ministry of Education
National & Local Joint Engineering Research Center for High-efficiency Display and Lighting Technology
School of Nanoscience and Materials Engineering
Collaborative Innovation Center of Nano Functional Materials and Applications
Henan University
Kaifeng 475004, P. R. China
E-mail: mengli@henu.edu.cn

G. Li, M. H. Aldamasy, L. Wang, A. Abate
Helmholtz-Zentrum Berlin für Materialien und Energie GmbH
Hahn-Meitner-Platz 1, 14109 Berlin, Germany
E-mail: guixiang.li.gl@gmail.com

The ORCID identification number(s) for the author(s) of this article can be found under https://doi.org/10.1002/adma.202407433

DOI: 10.1002/adma.202407433

J. Pascual
POLYMAT
Centro Joxe Mari Korta Center
University of the Basque Country UPV/EHU
Tolosa Avenue, 72, Donostia-San Sebastián 20018, Spain

Z. Su, J. Zhang, X. Gao
Shanghai Synchrotron Radiation Facility (SSRF)
Shanghai Advanced Research Institute
Chinese Academy of Sciences
239 Zhangheng Road, Shanghai 201204, P. R. China

S.-H. Turren-Cruz
Instituto de Ciencia de los Materiales (ICMUV)
Universidad de Valencia
C/Catedrático José Beltrán 2, Paterna E-46980, Spain

R. Roy, M. Saliba
Institute for Photovoltaics
University of Stuttgart
Pfaffenwaldring 47, 70569 Stuttgart, Germany

F. A Alharthi, A. Alsalme
Department of Chemistry
College of Science
King Saud University
Riyadh 11451, Kingdom of Saudi Arabia

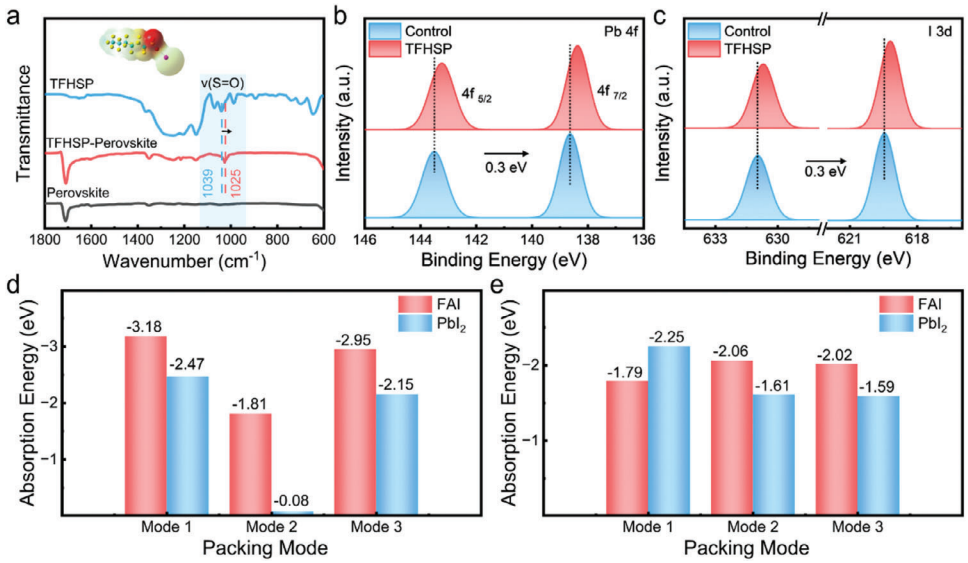

Figure 1. Interactions between TFHSP and perovskites. a) The molecular structure of TFHSP, along with FTIR spectra of TFHSP, and perovskite films with/without TFHSP treatment. XPS peaks of b) Pb 4f and c) I 3d of control and TFHSP-modified perovskite films. d) Absorption energies of single molecule in three different packing modes. e) Average absorption energies of six molecules in three different packing modes.

p-i-n devices losses has been significantly suppressed through the utilization of self-assembled monolayers.[6–8] Meanwhile the upper surface of perovskite still suffers from interface-induced nonradiative recombination due to high defect density and the unfavorable energy level alignment between perovskite and ETLs.[9,10]

Surface defects are well-known to cause nonradiative recombination centers, leading to losses in open-circuit voltage (V_{OC}) and fill factor (FF), ultimately impacting device performance. Meanwhile, these defects also serve as entry points for moisture, oxygen, and light-induced degradation,[11] negatively affecting device stability. Various strategies have been explored to reduce the number of defects and inhibit nonradiative recombination.[12–15] In addition to reduce defect density, strong chemical coordination at perovskite surfaces can form a physical barrier, decreasing the sensitivity to external environmental factors and thereby slowing down or even suppress the degradation of solar cells during operation.[16–18] Moreover, the unfavorable energy level alignment between perovskite surface and ETL (e.g., C_{60}) results in the accumulation of charges at the interface, affecting charge carriers transport. As stated by Chen et al., the driving force for charge carrier separation and extraction originates from the intrinsic electric field of the perovskite.[19] Inducing a stable dipole layer on the perovskite surface can optimize the energy level alignment, effectively enhancing the intrinsic electric field to aid charge extraction, and reducing charge accumulation.[20,21] Therefore, it is crucial to develop a multifunctional approach that both minimizes the detrimental impact of defects and optimizes interface energetics to achieve efficient and stable PSCs.

In this work, we report an effective strategy of "interfacial dipole engineering" by introducing a multifunctional tridecafluorohexane-1-sulfonic acid potassium salt dipole interlayer between perovskite and ETL to reduce interface-induced nonradiative recombination for high-performance p-i-n PSCs. We reveal a significant performance improvement in the device, originating from a more favorable energy level arrangement, reduced carrier recombination, and passivated interface defects for efficient carrier extraction. With the assistance of density functional theory (DFT) calculations, TFHSP exhibited an orderly vertical arrangement on the surface of perovskites and reacted with different terminated perovskite surfaces to passive the defects through coordination and hydrogen bonding interactions. Additionally, charge density difference analysis revealed a significantly reduced interfacial charge accumulation. The modified devices achieved 24.6% efficiency, negligible hysteresis, and excellent stability under operation and against atmospheric agents. Thus, dipole interface engineering is demonstrated as a viable technique with great potential for the development of high-performance perovskite devices.

2. Result and Discussion

TFHSP, illustrated in **Figure 1a**, contains multiple functional groups. The terminal sulfonate group (SO_3^-) can anchor the undercoordinated Pb^{2+} ions in the perovskite structure. The hydrophobic -CF_3 groups effectively inhibit the ingress of water and oxygen.[22] Additionally, K^+ ions can passivate interstitial defects by binding with halogen ions, thus inhibiting halide ion migration.[23] We applied TFHSP onto the surface of the perovskite through a simple post-processing approach (Figure S1, Supporting Information). Figure S2 (Supporting Information) shows the EDS element profile of the treated perovskite film, indicating that TFHSP is evenly distributed on the surface. In Figure S3 (Supporting Information), the scanning electron microscope (SEM) image of the control perovskite film reveals some voids, which create potential shunting paths and nonradiative recombination centers that would accelerate the device degradation.[23–25] Conversely, the surface of the TFHSP-treated film showed a compact surface, indicating that TFHSP has the

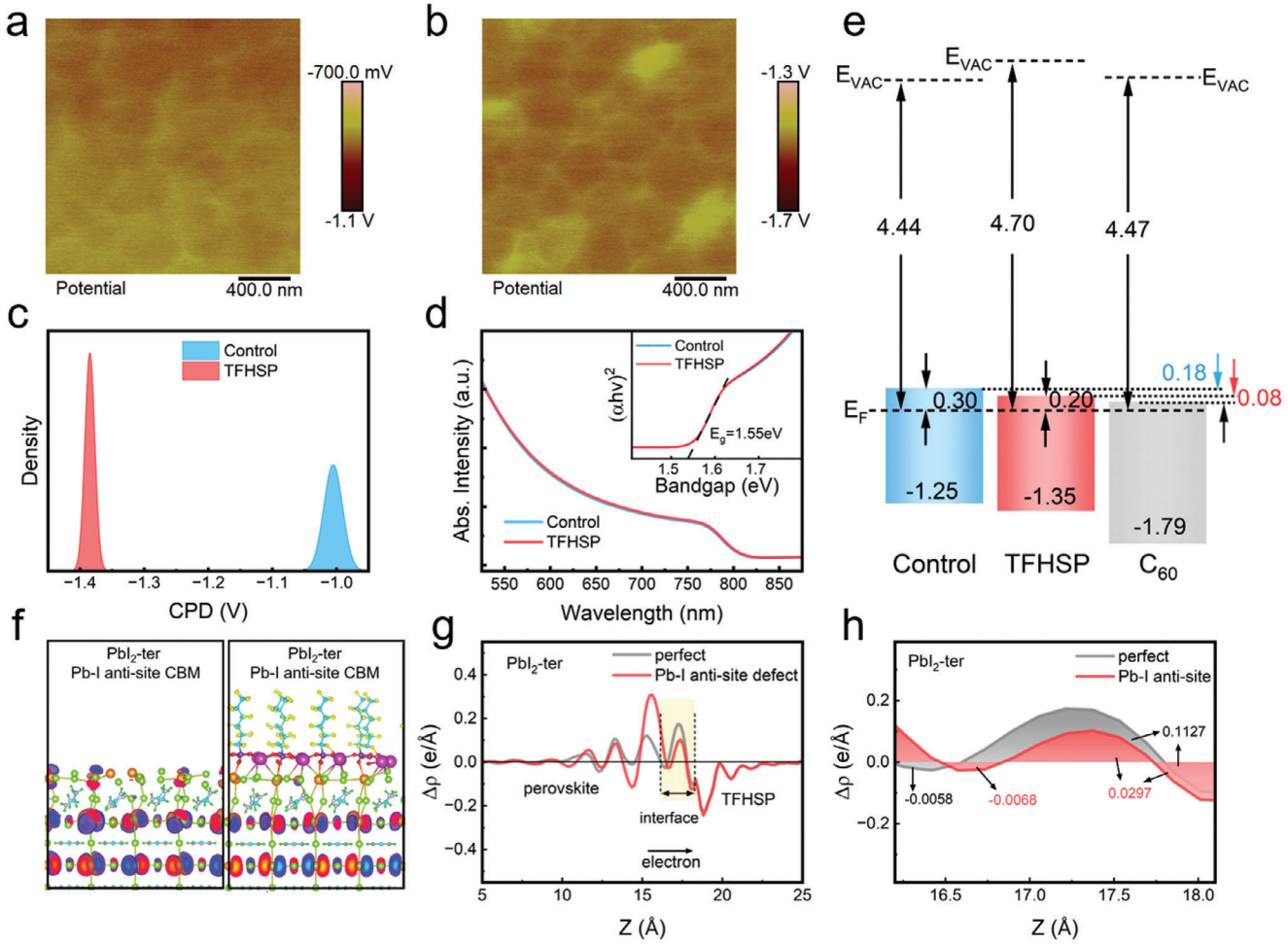

Figure 2. Electronic Properties and Interfacial Interaction. KPFM images of a) control and b) TFSHP perovskite films. (The concentration of TFHSP is 1 mg mL^{-1}). c) Potential distribution of control and TFHSP perovskite films. d) UV–vis and Tauc plot of control and TFHSP perovskite films. e) Energy level alignment of perovskite film and C_{60} layer. f) The charge density difference of TFHSP adsorbed on PbI_2-terminated perovskite (001) surface. g) Planar-averaged $\Delta\rho$ and h) enlarged Planar-averaged $\Delta\rho$ for perovskite-TFHSP on PbI_2-terminated surface. The Y-axis represents the accumulation (+) and depletion (-) of charges, while the X-axis represents the position corresponding to the perovskite-TFHSP interface. The gray line represents a perfect interface, and the red line represents an interface with Pb-I anti-site defects.

potential to reconstruct and improve the film morphology due to its ability to bind perovskite components. In Figure S4 (Supporting Information), the treated film displayed a root-mean-square (RMS) roughness of 17.2 nm, corresponding to a flatter surface, lower than 19.1 nm of the initial film. A smoother, less defective surface can improve the contact between the perovskite and the charge selective layer, facilitating charge transport.[12,26] To more accurately investigate the crystal structure and orientation of perovskites, we conducted X-ray diffraction (Figure S5, Supporting Information) and two-dimensional (2D) grazing-incidence wide-angle X-ray scattering (GIWAXS). As shown in Figures S6 and S7 (Supporting Information), the treated film shows stronger diffraction peaks and narrower full width at half maxima (FWHM), indicating improved perovskite crystallinity by TFHSP treatment.[27]

We further investigated the interaction between the TFHSP molecule and perovskite. From the Fourier transform infrared spectroscopy (FTIR) shown in Figure 1a, we observed S=O stretching vibration at 1039 cm^{-1} in the TFHSP molecule. When TFHSP was combined with perovskite, the S=O stretching vibration peak shifted to 1025 cm^{-1}, indicating the coordination between TFHSP and the perovskite components. In particular, S=O groups have the potential to donate electrons to the empty orbital of undercoordinated Pb^{2+}, thus chelating Pb^{2+} ions.[28,29] The interaction between TFHSP and perovskite was further confirmed by X-ray photoelectron spectroscopy (XPS). The XPS spectra of F 1s shown in Figure S8 (Supporting Information) indicate the presence of passivator molecules on the surface of perovskite films. In Figure 1b, the Pb $4f_{5/2}$ and Pb $4f_{7/2}$ XPS peaks for the treated perovskite film appear at 143.5 and 138.6 eV, respectively, which means a shift of 0.3 eV toward lower binding energy compared with the control perovskite. In Figure 1c, the binding energy of I 3d exhibits a similar trend. We attribute the decreased binding energy to defect passivation and electron donation by oxygen atoms in the SO_3^- group.[29]

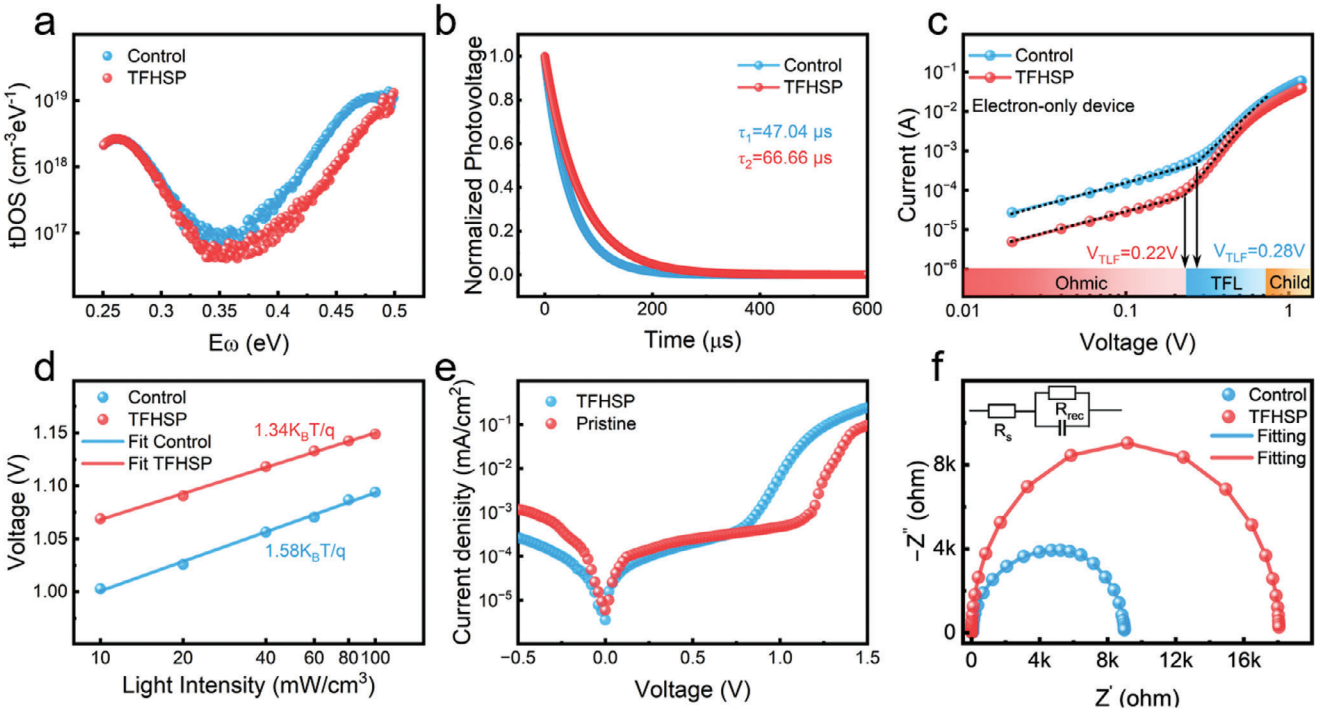

Figure 3. Optoelectronic Properties of Perovskite Films/Devices. a) Trap density of states (tDOS) spectra of devices with/without TFHSP treatment. b) TPV of devices with/without TFHSP treatment, τ_1 and τ_2 represent the charge carrier recombination lifetime of the control and TFHSP-treated devices. c) The trap densities of electron-only devices with/without TFHSP treatment, along the ohmic, trap-filled limit (TFL) and Child regions. d) Light intensity-dependence V_{OC} of devices with/without TFHSP treatment. e) Dark J–V curves of PSCs with/without TFHSP treatment. f) EIS characteristics of devices with/without TFHSP treatment.

To clarify the interaction mechanism between the TFHSP molecule and perovskite, we conducted DFT calculations. We constructed three types of molecular packing modes (Figure S9, Supporting Information): Mode 1 involves a vertical arrangement with the SO_3K group oriented toward the perovskite, Mode 2 involves a vertical with the CF_3 group oriented toward the perovskite, and Mode 3 involves a parallel arrangement. The detailed adsorption energy statistics are shown in Figure 1d. For FAI-terminated surface, the absorption energies of three packing modes are −3.18, −1.81, and −2.95 eV respectively. In the case of the PbI_2-terminated surface, the adsorption energies of three packing modes are −2.47, −0.08, and −2.15 eV, respectively, with Mode 1 exhibiting the lowest adsorption energy, indicating that TFHSP tends to bind with perovskite through the terminal SO_3K group. As shown in Figure S10 (Supporting Information), to further optimize the stacking configuration, we stacked six molecules onto the perovskite surface, and the average adsorption energies statistics are presented in Figure 1e. By comparing adsorption energies, we found that adsorption Model 1 is more stable in terms of energy, consistent with the adsorption results of a single molecule on the perovskite surface. Therefore, TFHSP exhibits an orderly vertical arrangement on the perovskite surface, with the SO_3K facing toward the perovskite surface. For the FAI-terminated surface, TFHSP establishes hydrogen bonding interactions between FAI via SO_3...H, with an O-H distance of 1.796 Å, consistent with NMR measurements (Figure S11, Supporting Information). For the PbI_2-terminated surface, TFHSP forms coordination bonds with undercoordinated Pb^{2+} ions.

We used a Kelvin probe microscope (KPFM) to measure the potential distribution of TFHSP-treated films, as shown in **Figure** 2a,b. After the TFHSP treatment, the surface potential decreased by approximately 0.4 eV and became more uniform (Figure 2c). Figure S12 (Supporting Information) shows the potential distribution of perovskite films treated with different concentrations of TFHSP, allowing for the statistical calculation of the shift in the surface work function (WF). We observed that TFHSP treatment improves the surface WF of the perovskites, which increases with TFHSP concentration (Figure S13, Supporting Information). When the concentration reaches 2 mg mL^{-1}, the surface WF shift reaches its highest value of ≈0.42 eV. Due to the strong electronegativity of F atoms, TFHSP molecules can induce the formation of interfacial dipoles on the perovskite surface, shifting the surface WF of the perovskite (Figure S14, Supporting Information).[18,21] We further carried out the UV–vis absorption measurements to examine the effect of interface modification on optical absorbance, displayed in Figure 2d. The optical absorption and bandgap of the treated sample remained unchanged, maintaining bandgap of 1.55 eV. To investigate the conduction band offset (CBO) between perovskite and C_{60} layers, we determined the energy level alignment of perovskite films before and after TFHSP treatment by ultraviolet photoelectron spectroscopy (UPS). The secondary electron cutoff and valence band spectra are shown in Figure S15 (Supporting Information), and the obtained energy level alignment is depicted in Figure 2e. Under open-circuit conditions, a higher CBO leads to the accumulation of a higher concentration of

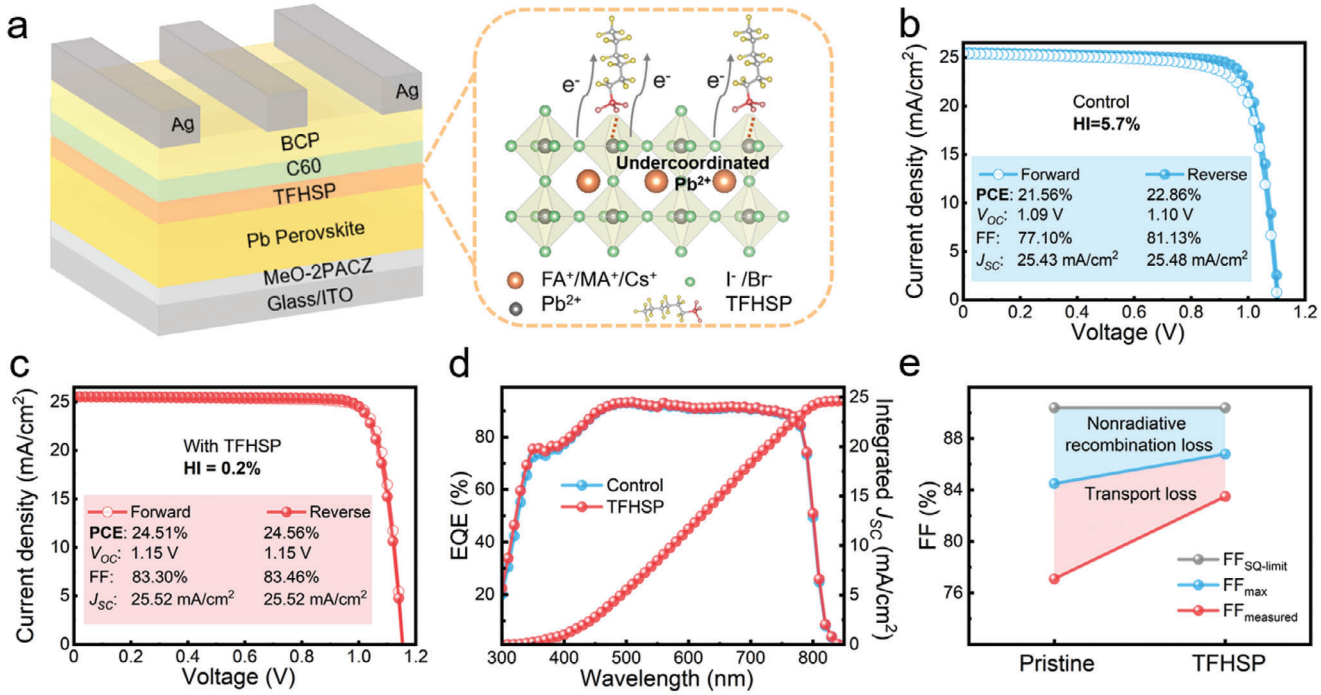

Figure 4. Device PV performances. a) Schematic of device structure and the interaction of TFHSP with perovskites. *J–V* curves of the champion PSCs for b) control and c) TFHSP. d) EQE spectra and integrated J_{SC} of the champion PSCs for control and TFHSP. e) Impact of charge transport and nonradiative recombination losses on FF for control and TFHSP devices.

electrons and holes near the interface after charge separation, resulting in severe charge recombination at the interface.[5] The shift between the conduction band minimum (CBM) offset of control perovskite and the lowest unoccupied molecular orbital (LUMO) of C_{60} is 0.18 eV. After TFHSP treatment, the CBO shift decreases to 0.08 eV, indicating less charge loss. The ionization energy (I*), which reflects the difference between the valence band maximum (VBM) of perovskite and the vacuum level, is used to indicate the degree of surface polarization. A higher I* implies more positive dipole moments, which is beneficial for the perovskite/C_{60} interface.[30,31] The I* of the control perovskite was 5.69 eV, and after TFHSP treatment, it increased by 0.35 eV. The reduction in interface losses after TFHSP treatment is attributed to the WF shift caused by the induced positive dipoles. This reduction in CBO decreases the accumulation of charge carriers at the interface, which would lead to an improvement in the V_{OC} of devices.[21]

To investigate the interface charge transfer characteristics, we calculated the charge distribution and differential charge density of Mode 1: six-molecule stacked perovskite surface structure. Additionally, we constructed a common deep-level defect, the Pb-I anti-site defect,[32] in the perovskite to evaluate the passivation effect of TFHSP. This approach allowed us to analyze the effectiveness of TFHSP in mitigating interface defects and improving charge transfer properties. Figure 2f and Figure S16 (Supporting Information) reveal the electron cloud localization in Pb-I anti-site defect structures before and after TFHSP passivation. After TFHSP passivation, the electron cloud becomes delocalized across the entire interface, indicating that the introduction of TFHSP eliminates the electronic states caused by Pb-I anti-site defect and achieves effective defect passivation. The charge distribution analysis indicates that for the FAI-terminated surface, the charge transfer numbers for the Pb-I anti-site defect and the defect-free interface with TFHSP are 5.26 e and 6.36 e, respectively. For the PbI_2-terminated surface, the charge transfer numbers are 4.03 e and 3.92 e, respectively. These values suggest that TFHSP treatment possesses high charge extraction efficiency. Subsequently, as shown in Figure 2g and Figure S17a (Supporting Information), the region with the most significant charge density variation is concentrated at the interface, with decreased charges in the region away from the interface. The charge integration at the interface shown in Figure 2h, highlights the reduced charge accumulation after TFHSP modification on the PbI_2-terminated surface, indicating the excellent passivation capability of this dipole molecule. Similarly, the reduction of charge accumulation by TFHSP is observed for the FAI-terminated surface with Pb-I anti-site defects (Figure S17b, Supporting Information). Lower charge accumulation is highly preferred, as it can lead to reduced device hysteresis.[33]

We performed thermal admittance spectroscopy to investigate the defect distribution in PSCs.[34] As shown in **Figure 3a**, the tDOS was plotted as a function of energy level depth. Compared to the control device, the TFHSP-modified device exhibited a significantly reduced defect density, particularly for deep-level defects at grain boundaries and surfaces. This suggests that TFHSP has a strong passivating ability of undercoordinated Pb^{2+} and Pb-I anti-site defects, consistent with DFT computational results.

The transient photovoltage (TPV) and transient photocurrent (TPC) were conducted to comprehensively analyze the charge carrier lifetime and charge carrier extraction properties.[34] As

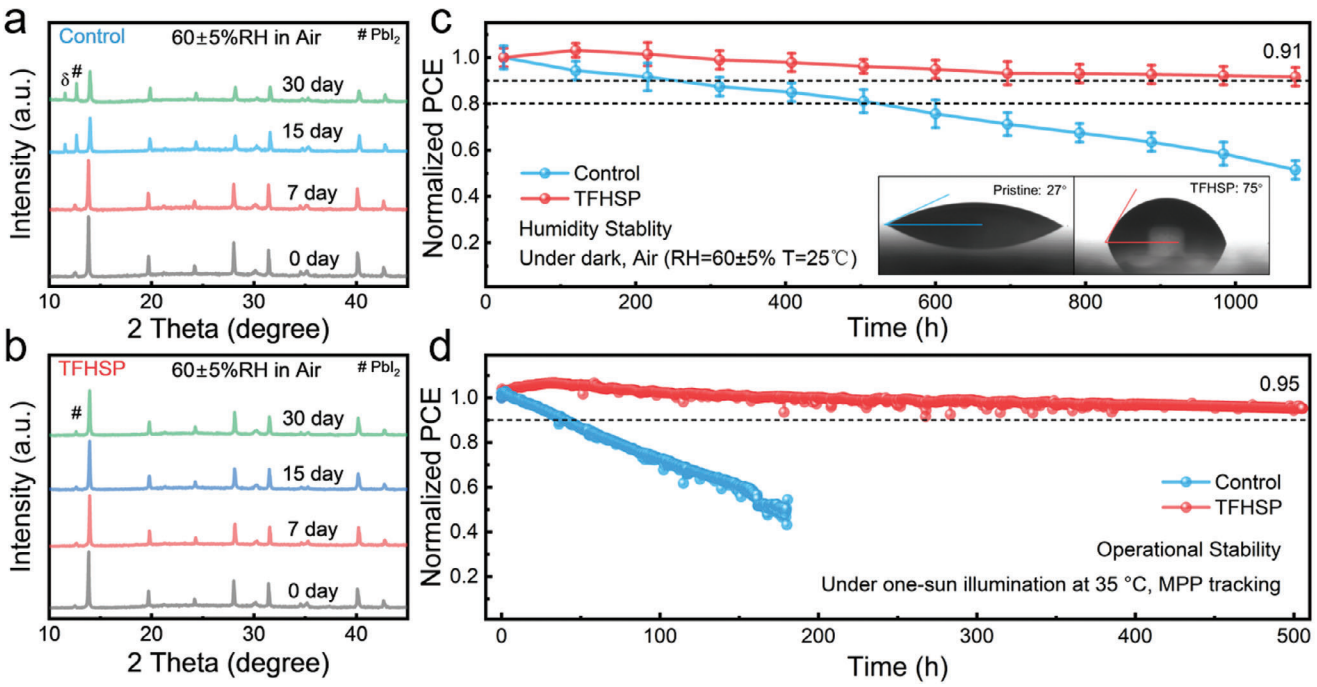

Figure 5. Long-term stability assessment of PSCs under different conditions. XRD patterns of perovskite films of a) control and b) TFHSP. c) Humidity stability of PSCs under high humidity conditions (60 ± 5% RH, 25 °C) inserted with water contact angles. d) Operational stability of PSCs under one-sun MPP tracking at 35 °C.

shown in Figure 3b, the charge carrier recombination lifetime for the TFHSP-modified device was 66.66 µs, higher than the control device's 47.04 µs, indicating that TFHSP treatment passivated the defects in the perovskite, efficiently suppressing nonradiative recombination. TPC is performed under short-circuit conditions (Figure S18, Supporting Information), showing that the charge transfer time for the TFHSP-modified device sample decreased from 2.98 to 1.48 µs, demonstrating faster charge transfer. As illustrated in Figure 3c, the defect state density of the device was investigated by the space charge limited current (SCLC) method, employing an electron-only device structure of ITO/TiO_2/Perovskite/C_{60}/Ag prepared for this analysis. The TFHSP-treated device shows lower electron trap density (1.12×10^{15} cm^{-3}) than that of the control device (1.42×10^{15} cm^{-3}), further verifying less nonradiative recombination and more efficient charge transport.[35]

To gain deeper insight into charge transport and carrier recombination dynamics, we investigated the dependence of V_{OC} and J_{SC} on the light intensity. As shown in Figure 3d, the slope of the V_{OC} versus the natural logarithm of light intensity for the control device is 1.58 K_BT/q, whereas for the TFHSP-modified device is 1.34 K_BT/q, indicating that the defect-induced SRH-recombination is inhibited.[13,22,36] A plot of J_{SC} versus illumination intensity in Figure S19 (Supporting Information) presents an exponential factor closer to 1 for the TFHSP-modified device, illustrating an improved interface charge drift and reduced charge recombination.[37–39] Figure 3e exhibited a reduction in reverse J_{SC} by an order of magnitude in the TFHSP-modified device compared to the control device. The lower dark current indicates fewer interface charge recombination and better interface contact. Additionally, the TFHSP-modified device exhibited a higher recombination resistance, as shown in Figure 3f, which is beneficial for reducing carrier recombination and improving charge transport.[40]

To verify the effect of the TFHSP treatment on device performance, the p-i-n devices with the structure ITO/MeO-2PACz/perovskite/C_{60}/BCP/Ag were prepared. As shown in **Figure 4a**, TFHSP can form coordination bonds with undercoordinated Pb^{2+} and facilitate charge extraction. The *J-V* curves of the champion TFHSP-treated and control PSCs, along with their corresponding photovoltaic parameters are shown in Figure 4b,c; Figures S20–S23 and Table S1 (Supporting Information). The control device exhibited a PCE of 22.86% with a V_{OC} of 1.10 V, while the TFHSP-treated device achieved PCE of 24.56% with V_{OC} of 1.15 V and FF of 83.46%. The improved PCE can be attributed to the inhibition of nonradiative recombination and the promotion of interfacial charge transport by TFHSP. The hysteresis index (*HI*) of the control device is 5.7%, while that of the modified device is only 0.2%, a remarkably low value seldom achieved among reports. The elimination of hysteresis can be attributed to a reduction in charge accumulation at the interface between the perovskite and TFHSP.[33] The external quantum efficiency (EQE) in Figure 4d shows that the integrated current density is consistent with the current density of the *J-V* curve. In Figure 4e, we calculated the impact of charge transport losses and nonradiative recombination losses on the FF. The maximum FF (FF_{max}) is estimated without considering charge transport losses.[41–43] The FF_{max} values of control and TFHSP-modified devices were 0.845 and 0.868, respectively, with differences of 0.074 and 0.033 from their actual FF values. The differences between the FF_{max} and SQ-limited ($FF_{SQ\text{-}limit}$) were 0.069 and 0.036 for the control and TFHSP-modified devices, respectively. The smaller

difference for the TFHSP devices indicates significantly suppressed nonradiative recombination and reduced carrier transport losses, contributing to the improvement of efficiency and stability.

As a crucial factor for commercialization, we investigated the operational stability of perovskite films and devices under different conditions. **Figure** 5a,b depicts the XRD changes of perovskite films placed in air with a relative humidity of 60% for 30 days. The untreated film underwent a noticeable phase transition, with decomposition after 15 days, showing a significant reduction in the (001) crystal plane and the formation of the δ phase and abundant PbI_2. After 30 days, decomposition becomes more severe. In contrast samples modified with TFHSP exhibit excellent moisture resistance. The control perovskite films were decomposed, showing PbI_2 even in an N_2-filled glovebox environment, while the TFHSP-modified films kept stable, indicating that the post-treatment with TFHSP effectively blocks intrinsic decomposition processes even in an inert atmosphere (Figure S24, Supporting Information). In the inset of Figure 5c, the treated film exhibits a contact angle of 75°, significantly higher than the untreated 27°. Additionally, we investigated the stability of the unencapsulated device in air with a 60% relative humidity. The TFHSP-modified devices maintained 91% of their initial efficiency for 1080 h, while the control devices decreased to 56% of their original PCE. We also observed a significantly higher storage stability for the treated devices when stored in the dark in an N_2 environment (Figure S25, Supporting Information). Furthermore, we evaluated the operational stability of the devices at the maximum power point (MPP). As shown in Figure 5d, the devices optimized with TFHSP maintained 95% of the initial efficiency after continuous illumination for 500 h at 35 °C, in contrast to the instability in the control device. Therefore, the stability of the device processed with TFHSP is greatly enhanced.

3. Conclusion

In summary, we reported an effective interfacial dipole engineering strategy by introducing a multifunctional dipole interlayer of TFHSP between perovskite and ETL. The treatment reduces interface-induced nonradiative recombination loss, achieving high-performance p-i-n PSCs. Through experimental investigation and theoretical analysis, we demonstrated that the introduction of TFHSP significantly reduces interface charge accumulation by inducing a stable positive layer and passivates surface defects via coordination and hydrogen bonding interactions. The TFHSP-treated device achieved a PCE of 24.6% and negligible hysteresis. Moreover, the devices exhibited outstanding humidity and operational stability. This work provides insights into understanding the interface charge behavior and offers a promising direction for achieving efficient and stable perovskite devices through dipole interface engineering.

Supporting Information

Supporting Information is available from the Wiley Online Library or from the author.

Acknowledgements

J.W. and R.Z. contributed equally to this work. The work was financially supported by the China Postdoctoral Science Foundation (No. 2022M721026), the Joint Fund of Provincial Science and Technology Research and Development Plan of Henan Province (No. 232301420004), Natural Science Foundation for Young Scientists of Henan Province (242300421069) and the National Natural Science Foundation of China (No. 22103022). and Henan Postdoctoral Sustentation (20213036). R.Z. thanks for the support of the computational resources provided by the Harbin Supercomputer Center. The authors are thankful for beamline BL14B1 and BLO3HB at the Shanghai Synchrotron Radiation Facility (SSRF) for providing the beam time. S.T. is thankful for the funding support of Ministry of Science and Innovation of Spain under Ayudas Ramón y Cajal (RYC2022-035578-I).

Conflict of Interest

The authors declare no conflict of interest.

Author Contributions

G.L. and M.L. conceived the idea. J.X. and M.L. designed the experiments. J.W., G.L., Z.Z., H.W., L.W., and M.L. fabricated and characterized perovskite films and devices. Z.S. and X.G. conducted the GIWAXS measurements, J.Z. conducted the XPS and UPS measurements, R.Z. performed the theoretical calculation. J.W., G.L., and M.L. participated in the data analysis and result discussions. J.W. composed the manuscript. G.L., J.P., M.A., S.T., R.R., F.A., A.A., M.S., A.A., and M.L. contributed to suggestions for the manuscript. G.L., A.A., and M.L. provided expertise and supervised the work. All authors reviewed the manuscript.

Data Availability Statement

The data that support the findings of this study are available in the supplementary material of this article.

Keywords

charge transport, dipole molecule, interfacial nonradiative recombination, perovskite solar cells (PSCs)

Received: May 24, 2024
Revised: June 30, 2024
Published online: July 7, 2024

[1] A. Kojima, K. Teshima, Y. Shirai, T. Miyasaka, *J. Am. Chem. Soc.* **2009**, *131*, 6050.
[2] H.-S. Kim, C.-R. Lee, J.-H. Im, K.-B. Lee, T. Moehl, A. Marchioro, S.-J. Moon, R. Humphry-Baker, J.-H. Yum, J. E. Moser, *Sci. Rep.* **2012**, *2*, 591.
[3] M. Kim, J. Jeong, H. Lu, T. K. Lee, F. T. Eickemeyer, Y. Liu, I. W. Choi, S. J. Choi, Y. Jo, H.-B. Kim, *Science* **2022**, *375*, 302.
[4] X. Li, X. Liu, X. Wang, L. Zhao, T. Jiu, J. Fang, *J. Mater. Chem. A* **2015**, *3*, 15024.
[5] H. Chen, A. Maxwell, C. Li, S. Teale, B. Chen, T. Zhu, E. Ugur, G. Harrison, L. Grater, J. Wang, *Nature* **2023**, *613*, 676.
[6] Q. Tan, Z. Li, G. Luo, X. Zhang, B. Che, G. Chen, H. Gao, D. He, G. Ma, J. Wang, *Nature* **2023**, *620*, 545.

[7] Z. Li, X. Sun, X. Zheng, B. Li, D. Gao, S. Zhang, X. Wu, S. Li, J. Gong, J. M. Luther, *Science* **2023**, *382*, 284.
[8] S. M. Park, M. Wei, N. Lempesis, W. Yu, T. Hossain, L. Agosta, V. Carnevali, H. R. Atapattu, P. Serles, F. T. Eickemeyer, *Nature* **2023**, *624*, 289.
[9] F. Ye, S. Zhang, J. Warby, J. Wu, E. Gutierrez-Partida, F. Lang, S. Shah, E. Saglamkaya, B. Sun, F. Zu, *Nat. Commun.* **2022**, *13*, 7454.
[10] C. Liu, Y. Yang, H. Chen, J. Xu, A. Liu, A. S. Bati, H. Zhu, L. Grater, S. S. Hadke, C. Huang, *Science* **2023**, *382*, 810.
[11] S. Yang, S. Chen, E. Mosconi, Y. Fang, X. Xiao, C. Wang, Y. Zhou, Z. Yu, J. Zhao, Y. Gao, *Science* **2019**, *365*, 473.
[12] D. L. McGott, C. P. Muzzillo, C. L. Perkins, J. J. Berry, K. Zhu, J. N. Duenow, E. Colegrove, C. A. Wolden, M. O. Reese, *Joule* **2021**, *5*, 1057.
[13] Q. Jiang, Y. Zhao, X. Zhang, X. Yang, Y. Chen, Z. Chu, Q. Ye, X. Li, Z. Yin, J. You, *Nat. Photonics* **2019**, *13*, 460.
[14] F. Yang, R. Zhu, Z. Zhang, Z. Su, W. Zuo, B. He, M. H. Aldamasy, Y. Jia, G. Li, X. Gao, *Adv. Mater.* **2024**, *36*, 2308655.
[15] G. Li, Z. Su, M. Li, F. Yang, M. H. Aldamasy, J. Pascual, F. Yang, H. Liu, W. Zuo, D. Di Girolamo, *Adv. Energy Mater.* **2021**, *11*, 2101539.
[16] Z. Li, B. Li, X. Wu, S. A. Sheppard, S. Zhang, D. Gao, N. J. Long, Z. Zhu, *Science* **2022**, *376*, 416.
[17] G. Li, Y. Hu, M. Li, Y. Tang, Z. Zhang, A. Musiienko, Q. Cao, F. Akhundova, J. Li, K. Prashanthan, *Angew. Chem., Int. Ed.* **2023**, *135*, 202307395.
[18] Z. Zhang, Z. Su, G. Li, J. Li, M. H. Aldamasy, J. Wu, C. Wang, Z. Li, X. Gao, M. Li, *Adv. Funct. Mater.* **2023**, *34*, 2306458.
[19] W. Chen, S. Liu, Q. Li, Q. Cheng, B. He, Z. Hu, Y. Shen, H. Chen, G. Xu, X. Ou, *Adv. Mater.* **2022**, *34*, 2110482.
[20] T. Li, J. Xu, R. Lin, S. Teale, H. Li, Z. Liu, C. Duan, Q. Zhao, K. Xiao, P. Wu, *Nat. Energy* **2023**, *8*, 610.
[21] L. Canil, T. Cramer, B. Fraboni, D. Ricciarelli, D. Meggiolaro, A. Singh, M. Liu, M. Rusu, C. M. Wolff, N. Phung, *Environ. Sci.* **2021**, *14*, 1429.
[22] J. Zhang, Z. Li, F. Guo, H. Jiang, W. Yan, C. Peng, R. Liu, L. Wang, H. Gao, S. Pang, *Angew. Chem.* **2023**, *135*, 202305221.
[23] D.-Y. Son, S.-G. Kim, J.-Y. Seo, S.-H. Lee, H. Shin, D. Lee, N.-G. Park, *J. Am. Chem. Soc.* **2018**, *140*, 1358.
[24] C. Sun, Y. Jiang, M. Cui, L. Qiao, J. Wei, Y. Huang, L. Zhang, T. He, S. Li, H.-Y. Hsu, *Nat. Commun.* **2021**, *12*, 2207.
[25] G. Li, Z. Su, L. Canil, D. Hughes, M. H. Aldamasy, J. Dagar, S. Trofimov, L. Wang, W. Zuo, J. J. Jerónimo-Rendon, *Science* **2023**, *379*, 399.
[26] T. Kong, H. Xie, Y. Zhang, J. Song, Y. Li, E. L. Lim, A. Hagfeldt, D. Bi, *Adv. Energy Mater.* **2021**, *11*, 2101018.
[27] Z. Xu, Z. Liu, N. Li, G. Tang, G. Zheng, C. Zhu, Y. Chen, L. Wang, Y. Huang, L. Li, *Adv. Mater.* **2019**, *31*, 1900390.
[28] X. Zheng, Y. Deng, B. Chen, H. Wei, X. Xiao, Y. Fang, Y. Lin, Z. Yu, Y. Liu, Q. Wang, *Adv. Mater.* **2018**, *30*, 1803428.
[29] J. Zhu, Y. Qian, Z. Li, O. Y. Gong, Z. An, Q. Liu, J. H. Choi, H. Guo, P. J. Yoo, D. H. Kim, *Adv. Energy Mater.* **2022**, *12*, 2200632.
[30] X. Y. Chin, D. Turkay, J. A. Steele, S. Tabean, S. Eswara, M. Mensi, P. Fiala, C. M. Wolff, A. Paracchino, K. Artuk, *Science* **2023**, *381*, 59.
[31] Z. Liu, H. Li, Z. Chu, R. Xia, J. Wen, Y. Mo, H. Zhu, H. Luo, X. Zheng, Z. Huang, *Adv. Mater.* **2024**, *36*, 2308370.
[32] B. Chen, P. N. Rudd, S. Yang, Y. Yuan, J. Huang, *Chem. Soc. Rev.* **2019**, *48*, 3842.
[33] S. Zhang, H. Si, W. Fan, M. Shi, M. Li, C. Xu, Z. Zhang, Q. Liao, A. Sattar, Z. Kang, *Angew. Chem.* **2020**, *132*, 11670.
[34] J. He, W. Sheng, J. Yang, Y. Zhong, Y. Su, L. Tan, Y. Chen, *Energy Environ. Sci.* **2023**, *16*, 629.
[35] S. Jeong, S. Seo, H. Yang, H. Park, S. Shin, H. Ahn, D. Lee, J. H. Park, N. G. Park, H. Shin, *Adv. Energy Mater.* **2021**, *11*, 2102236.
[36] W.-Q. Wu, Z. Yang, P. N. Rudd, Y. Shao, X. Dai, H. Wei, J. Zhao, Y. Fang, Q. Wang, Y. Liu, *Sci. Adv.* **2019**, *5*, eaav8925.
[37] Y. Su, J. Yang, G. Liu, W. Sheng, J. Zhang, Y. Zhong, L. Tan, Y. Chen, *Adv. Funct. Mater.* **2022**, *32*, 2109631.
[38] S. Xiong, Z. Hou, S. Zou, X. Lu, J. Yang, T. Hao, Z. Zhou, J. Xu, Y. Zeng, W. Xiao, *Joule* **2021**, *5*, 467.
[39] S. Shen, Y. Mi, Y. Ouyang, Y. Lin, J. Deng, W. Zhang, J. Zhang, Z. Ma, C. Zhang, J. Song, *Angew. Chem.* **2023**, *135*, 202316495.
[40] Y. Wu, B. Chang, L. Wang, H. Li, L. Pan, Z. Liu, L. Yin, *Adv. Mater.* **2023**, *35*, 2300174.
[41] M. A. Green, *Sol. Cells* **1982**, *7*, 337.
[42] J. Wang, J. Zhang, Y. Zhou, H. Liu, Q. Xue, X. Li, C.-C. Chueh, H.-L. Yip, Z. Zhu, A. K. Jen, *Nat. Commun.* **2020**, *11*, 177.
[43] T. Niu, W. Zhu, Y. Zhang, Q. Xue, X. Jiao, Z. Wang, Y.-M. Xie, P. Li, R. Chen, F. Huang, *Joule* **2021**, *5*, 249.